# Deep Low-Frequency Earthquakes Associated with the Eruptions of Shinmoe-dake in Kirishima Volcanoes

**Ryo Kurihara[1], Kazushige Obara[1], Akiko Takeo[1], and Yusaku Tanaka[1]**

[1] Earthquake Research Institute, the University of Tokyo

Corresponding author: Ryo Kurihara (rkuri@eri.u-tokyo.ac.jp)

**Key Points:**

- Activation of low-frequency earthquakes at depths of 20–27 km started one year before the 2011 eruptions of Shinmoe-dake.

- Waveforms of low-frequency earthquakes associated with the 2011 eruptions indicate lower dominant frequencies than those of the others.

- Activated low-frequency earthquake locations might have been switched by fluid path redistribution with eruption style transitions.

17    **Abstract**

18    Deep low-frequency (DLF) earthquakes occur beneath the Kirishima volcanoes in
19    southwest Japan at depths of 10–30 km. In this study, we aim to reveal the relationship between
20    DLF earthquakes and volcanic activity including eruptions by relocating the hypocenters of the
21    earthquakes using the network correlation coefficient method and detecting the earthquakes
22    comprehensively using the matched filter technique. Hypocenters of DLF earthquakes are
23    found to be concentrated in some separated small clusters within depths of 10–15 and 20–27
24    km. Activation of deeper DLF earthquakes had been observed for approximately two years
25    from December 2009, during which various styles of eruptions occurred. Such a two-year
26    increase in DLF seismicity was well correlated with crustal deformation because of the volume
27    change of a magma reservoir. The waveforms and hypocenters of DLF earthquakes during the
28    activation period were different from those during other time periods. The activated DLF
29    earthquakes mostly had low dominant frequencies and were located in four deeper clusters.
30    The activation of each cluster was switched three times at the transition of the eruption styles.
31    These results suggest that DLF earthquakes might occur near magma sills and could be
32    triggered by fluid flow in the changing paths by complex eruption processes. In addition, the
33    waveforms and hypocenters of DLF earthquakes associated with the 2018 eruptions are
34    different from those associated with the 2011 eruptions. The fluid paths of the 2018 eruptions
35    might be different from those of the 2011 eruptions.

36

37    **Plain Language Summary**

38    Deep low-frequency (DLF) earthquakes occur at depths of 10–30 km beneath the
39    Kirishima volcanoes, which is one of the most active volcanoes in Japan. In the last decade,
40    two major series of eruptions were observed there. The relationship between DLF earthquakes
41    and volcanic activity such as eruptions is still unknown; therefore, we conduct two analyses,
42    namely, relocation and detection to obtain the precise spatial distribution and comprehensive
43    temporal distribution of DLF earthquakes based on waveform correlations. The result is that
44    DLF earthquakes occurred in some small clusters, having been activated for approximately two
45    years from December 2009, during which various styles of eruptions including subplinian
46    eruptions on 26–27 January 2011 occurred. The long-term increase in DLF earthquakes was
47    well correlated with crustal deformation because of the volume change of the magma reservoir.
48    Most DLF earthquakes associated with the 2011 eruptions are distributed in four deeper
49    clusters which are different from those of DLF earthquakes in the other time periods. Moreover,
50    the clusters were switched three times, which approximately correlates with the transitions of
51    eruption styles. These results suggest that DLF earthquakes were triggered by fluid flow in the
52    deep crust related to the eruptions.

53

54

55

## 1 Introduction

We frequently observe anomalous microearthquakes with predominant frequencies of 1–10 Hz at depths of around 30 km in the Japan island arc whereas most of all the inland regular earthquakes occur at depths shallower than 15 km. The earthquakes are usually called as deep low-frequency (DLF) earthquakes. Japan meteorological agency (JMA) observes the DLF earthquakes, and the earthquakes are included in the seismic catalog of JMA [Katsumata and Kamaya, 2003]. The depth of 30 km for many DLF earthquakes is equivalent to the Moho discontinuity [Ukawa, 2007; Kosuga et al., 2017]; however, low-frequency earthquakes sometimes occur at depths from 10 to 50 km. In this study, we define low-frequency earthquakes deeper than 10 km as DLF earthquakes. DLF earthquakes are classified into three types based on their locations: tectonic DLF earthquakes occurring at plate subduction zones, volcanic DLF earthquakes occurring near volcanoes, and semi-volcanic DLF earthquakes occurring far from either of those [Aso et al., 2013]. Regardless of their location, waveforms of DLF earthquakes are similar to each other.

DLF earthquakes distributed near volcanoes can be a key to reveal the physical processes of volcanic activity, including eruptions, because DLF earthquake activity is supposed to be associated with eruptions. Ukawa and Ohtake [1987] reported that a DLF earthquake at a depth of approximately 30 km occurred before the 1986 eruption of Izu-Oshima volcano, Japan. White [1996] showed that DLF earthquakes occurred before the 1991 eruption of Pinatubo volcano, Philippines. Shapiro et al. [2017] and Frank et al. [2018] showed the relationship between DLF and long-period earthquakes near the surface beneath the Klyuchevskoy volcano group at Kamchatka, Russia. However, the relationship is still unknown in many other volcanoes. Takahashi and Miyamura [2009] analyzed DLF earthquakes all over Japan based on the JMA catalog and concluded that they could not find DLF earthquakes corresponding to surface volcanic activity such as eruptions.

DLF earthquakes are considered to be affected by fluid movements in a volcanic area [Aki and Koyanagi, 1981; Hensch et al., 2019]. DLF earthquakes occur around the low velocity and low Q zones possibly because of the existence of fluid [Hasegawa et al., 2005]. At Laacher See volcano in Germany, migration of magma or magmatic fluid may be related to DLF earthquakes and it suggests recharge of magma chamber [Hensch et al., 2019]. Hotovec-Ellis et al. [2018] reported similar results derived at Mammoth Mountain California, USA. The above fluid model is supported by studies on focal mechanisms of DLF earthquakes. Nakamichi et al. [2003] revealed that DLF earthquakes at Iwate volcano in northeastern Japan have focal mechanisms including compensated-linear-vector-dipole (CLVD) components, which suggests existence of fluid movement. Aso and Tsai [2014] proposed the cooling magma model in which DLF earthquakes are considered to be triggered by thermal strain.

Kirishima volcanoes located in the southern part of Kyushu island includes three active volcanoes—Shinmoe-dake, Io-yama, and Ohachi. Shinmoe-dake has been one of the most active volcanoes in Japan over the past few decades. In fact, it erupted several times in 2008–2011 and 2017–2018. Phreatic eruptions as precursory activity occurred in 2008–2010 [Suzuki et al., 2013], subplinian eruptions occurred on 26–27 January 2011, vulcanian eruptions occurred in February and April 2011, and phreatomagmatic eruptions occurred from June to September 2011 [Nakada et al., 2013]. Shinmoe-dake also erupted in October 2017 and March–April 2018. Io-yama, located northwest of Shinmoe-dake, erupted in April 2018 as well [Japan Meteorological Agency, 2018]. In Kirishima volcanoes, volcanic DLF earthquakes occur at depths of approximately 10–15 km and 20–27 km, according to the JMA catalog. In the vicinity of these DLF earthquakes, low velocity zones at depths of 5–15 and 25–35 km have been imaged by tomography and seismic interferometry [Yamamoto and Ida, 1994; Nagaoka et al.,

104    2018; Zhao et al., 2018]. However, DLF seismicity associated with eruptions has not been
105    observed in Kirishima volcanoes up to now.

106         We aim to reveal the relationship between DLF earthquakes and volcanic activity in
107    this study. For this purpose, precise locations of DLF earthquakes and a comprehensive catalog
108    of earthquakes are necessary. However, the JMA catalog includes errors of locations, which
109    make it insufficient for that purpose, because the waveforms of the DLF earthquake are
110    complicated, and the onsets of P and S waves are unclear. Thus, to obtain precise locations and
111    a comprehensive catalog of DLF earthquakes, we use the network correlation coefficient
112    method [Ohta and Ide, 2011] and the matched filter technique [Gibbons and Ringdal, 2006;
113    Shelly et al., 2007]. Then, we show the results of the analyses, indicating increases in DLF
114    earthquakes associated with eruptions in Kirishima volcanoes. In addition, we classify DLF
115    earthquakes and find characteristic types of DLF earthquakes which mainly occur with
116    eruptions.
117
118

## 2 Data and Methods

119

120      In this study, we use the network correlation coefficient (NCC) method and the matched
121  filter technique (MFT). For both analyses, we use three-component seismograms of the high-
122  sensitivity seismograph network (Hi-net), operated by the National Research Institute for Earth
123  Science and Disaster Resilience (NIED) [Okada et al., 2004; NIED, 2019] after applying a
124  band-pass filter of 1−4 Hz.

125      To relocate the hypocenters of DLF earthquakes in the JMA catalog, we adapt the NCC
126  method, which was originally used for tectonic DLF earthquakes in the Nankai subduction
127  zone [Ohta and Ide, 2011]. NCC refers to the summed correlation coefficients between two
128  waveforms of one earthquake pair calculated over many stations. In this method, the relative
129  locations of each earthquake pair are estimated by maximizing the NCC on a grid search. We
130  use the 100-Hz sampling data of velocity waveforms observed at 10 Hi-net stations (Figure 1).
131  We apply this method to all of the 275 DLF earthquakes that occurred from April 2004 to
132  December 2015 in the JMA catalog. The length of the time window is 5 s, and the estimated
133  arrival time is at the center of the time window. Estimated arrival time is calculated by using
134  P- and S-wave velocities for vertical and horizontal components, respectively. To reduce error
135  in the locations, we exclude the earthquakes whose correlations between them and the other
136  earthquakes are less than six times the standard deviations of NCCs for various assumptions of
137  relative relocation.

138      To make a comprehensive catalog of DLF earthquakes, we apply MFT [Gibbons and
139  Ringdal, 2006; Shelly et al., 2007]. In this method, DLF earthquakes are detected when the
140  summed correlation coefficients (CC) of waveforms at many stations are higher than the
141  detection threshold. The period of the analysis is from April 2004 to December 2018. We first
142  decimate the Hi-net data from 100 Hz to 12.5 Hz to reduce the computational cost. Time
143  windows of 5 s are used, and the centers of the time windows correspond to the estimated
144  arrival times of S waves in all  components. We select 200 template DLF earthquakes with
145  high signal to noise ratios (SN ratios) from the JMA catalog and use three components of six
146  Hi-net stations, which show high SN ratios. When the data of one or two observation stations
147  are missing for the target day, we add the same amount of data from the other stations that are
148  used for relocation as well. The maximum value of the summed CC is always 18. The detection
149  threshold of summed CC is set to 5.5, equivalent to approximately 11 times of median absolute
150  deviations (MAD). This value is higher than eight times of MAD, used for analysis of tectonic
151  DLF earthquakes [Shelly et al., 2007], to prevent misdetection. After detection, we select the
152  one detected earthquake that has the highest summed CC in 10-s time window to avoid multiple
153  counting of one DLF earthquake.

154      Regardless of our severe threshold, misdetections sometimes occur because the number
155  of stations is limited, and the SN ratios of waveforms are usually low. To reduce misdetections
156  more, we use CC and estimated magnitudes calculated based on template DLF earthquakes by
157  the following equation

158         $Mj_\text{detect} = Mj_\text{temp} + \frac{1}{0.85}\log\left(\frac{V_\text{detect}}{V_\text{temp}}\right)$ ・・・(1)

159  where $Mj_\text{detect}$ and $Mj_\text{temp}$ are the JMA magnitudes of the detected DLF earthquake and the
160  template earthquake, respectively. $V_\text{detect}$ and $V_\text{temp}$ are the maximum values of velocities in
161  the time windows of 5 s. We use three-component data from the N.SUKH station to calculate
162  magnitude. The 0.85 is obtained by the equation used to estimate the magnitude in JMA
163  [Funasaki and Earthquake Prediction Information Division, 2004]. We distinguish detected
164  DLF earthquakes from misdetections based on the following procedure. First, we select as DLF
165  earthquakes only the events whose summed CC are larger than 7.0. Next, we remove those

166　with large magnitudes because they may reflect the surface waves of regular earthquakes. The
167　threshold of the magnitudes is calculated based on the DLF earthquakes selected above. Events
168　are determined as misdetections when the magnitudes of the events with summed CC between
169　5.5 and 7.0 are larger than the magnitude of the top three percent DLF earthquakes, which is
170　equal to magnitude 0.9. The magnitudes of some events cannot be calculated because the
171　magnitudes of some template earthquakes were not determined by JMA. We do not use the
172　threshold of magnitude for such detected events. Finally, to reduce misdetections by noise such
173　as wind or microseisms, we use the spectrum ratios of 2.0–4.0 Hz to 0.5–1.0 Hz at the N.NRAH
174　station, which shows the highest SN ratio values in the template events. We remove the events
175　whose summed CC are between 5.5 and 7.0 and spectrum ratios are less than 0.2. In other
176　words, we remove the events with large energy on the 0.5–1.0-Hz band, which is lower than
177　the dominant frequency of DLF earthquakes, 1.0–10.0 Hz.

178　**3 Locations of DLF earthquakes**

179　　　　Figure 2a shows the locations of DLF earthquakes in the Kirishima volcanoes in the
180　JMA catalog. One unique characteristic of these earthquakes is that there is a seismic gap at a
181　depth of 15–20 km. In other words, the hypocenters are separated into a shallow spot at a depth
182　of 10–15 km and a deep spot at a depth of 20–27 km, while the hypocenters of DLF earthquakes
183　in most of the other volcanoes have continuous distributions in the vertical direction according
184　to the JMA catalog. Both spots are above the Moho discontinuity in the Kirishima volcanoes
185　at the depth of approximately 30 km here [Matsubara et al., 2017].
186　　　　We obtain new locations of 201 DLF earthquakes from 275 earthquakes in the JMA
187　catalog by NCC method. Relocated hypocenters are also separated into both shallow and deep
188　spots. Unlike the original catalog of the JMA, the hypocenters are concentrated in some smaller
189　clusters (Figure 2b). In other words, DLF earthquakes are not distributed continuously in the
190　vertical direction but are located in isolated small clusters. Beneath the Ohachi volcano, the
191　hypocenters are concentrated at depths of approximately 12 and 14 km. Most of the DLF
192　earthquakes that occurred deeper than 20 km were concentrated in the largest cluster at a depth
193　of 22 km, while some earthquakes are located in small clusters at depths of 25–27 km. The
194　DLF earthquakes deeper than 20 km are located in the north of Ohachi (Figure 2b).
195　　　　The errors of the relocation are difficult to estimate because the NCC method does not
196　use the linear equation. However, the errors may be less than few kilometers and we find the
197　difference of DLF seismicity by the depths even if the distance between the earthquakes are
198　smaller than a few kilometers, as discussed in next section.
199

200　**4 Activities of DLF earthquakes corresponding to the eruptions**

201　4.1 Temporal distribution of DLF earthquakes
202　　　　From April 2004 to December 2018, 2964 DLF earthquakes were detected by MFT.
203　The number of detected DLF earthquakes is approximately 10 times as large as that in the
204　JMA catalog. Newly detected DLF earthquakes mainly consist of small magnitude
205　earthquakes and magnitude-frequency distributions of the earthquakes follow the Gutenberg–
206　Richter law (Figure S1). Cumulative numbers of DLF earthquakes in the JMA catalog and
207　MFT catalog are shown in Figure 3. DLF earthquakes in the JMA catalog occurred constantly
208　(Figure 3b) but those in the MFT catalog increased significantly between end of 2009 and
209　late 2011 (Figure 3).
210　　　　Around the 2011 subplinian eruptions, long-term increase of DLF earthquakes for
211　about two years and swarms of DLF earthquakes in few days are observed (Figure 4). The
212　two-year increasing seismicity from December 2009 to September 2011 is commonly

213 observed for DLF earthquakes with all ranges of magnitude (Figure S2). Swarms of DLF
214 earthquake are observed in August 2010, December 2010 and February 2011. Although
215 swarms of DLF earthquakes mainly consist of small events, the swarms which include small
216 number of DLF earthquakes are also observed with all ranges of magnitude (Figure S3).
217 There is no significant activation of DLF earthquakes directly corresponding to the
218 subplinian eruptions on 26–27 January 2011. After the swarm of DLF earthquakes in
219 February 2011, the long-term increase in DLF earthquakes had gradually finished by the end
220 of 2011.
221     DLF earthquakes are generally separated into two spots shallower and deeper than the
222 depth of 17 km (see Figure 2). Most DLF earthquakes detected by MFT are located in the
223 deeper spot (Figures 3e) while number of those in the shallower spot is smaller than 200
224 without significant activations near the 2011 eruptions (Figure 3d).
225     The seismicity of DLF earthquakes from December 2009 is correlated with crustal
226 deformation. Figures 3a and 4a show the amount of the radial component of horizontal
227 displacement of Ebino relative to Makizono (see Figure 1), calculated from GNSS data (F3
228 solutions) provided by the Geospatial Information Authority of Japan. These two stations show
229 the largest relative horizontal displacement which probably reflects the volume change in the
230 magma reservoir located near Io-yama (yellow star in Figure 1) at a depth of 8 km [Nakao et
231 al., 2013]. The trend of horizontal displacement also changed at the end of 2009, when DLF
232 earthquakes increased, and the extension trend corresponded to the 2011 eruptions of Shinmoe-
233 dake. The change in the trend lasted until the end of 2011, except for the shortening by the
234 eruptions in January 2011.
235     After the sequence of DLF earthquakes associated with the 2011 eruptions, another
236 small activation of DLF earthquakes was observed after September 2017 (Figure 3c). This
237 increase is also correlated with the eruptions of Shinmoe-dake and Io-yama that occurred in
238 October 2017 and in March–April 2018. This increase is observed in the JMA catalog as well.
239 The horizontal displacement is also extended in this period.
240
241 *4.2 Classification of DLF earthquakes*
242
243     To investigate the activations of DLF earthquakes, we attempt to classify the DLF
244 earthquakes. However, it is difficult to classify them based on the relocated hypocenters
245 because most DLF earthquakes are located in the largest cluster at a depth of 22 km (Figure 2).
246 Thus, we classify DLF earthquakes based on the period in which the detected earthquakes are
247 concentrated.
248     First, to classify template DLF earthquakes, we determine the concentration ratio (CR)
249 of each template earthquake as follows:

250 $$CR_i(T_{\text{start}}, T_{\text{end}}) = \frac{N_i(T_{\text{start}} < t < T_{\text{end}})}{N_i^{\text{total}}} \qquad \cdot\cdot\cdot (2)$$

251 where $N_i^{\text{total}}$ refers to the total number of detected earthquakes by the $i$ th template in all periods
252 of analysis, which is from April 2004 to December 2018. $T_{\text{start}}$ and $T_{\text{end}}$ show the start times
253 and end times of the periods defined in Table 1. We consider three periods corresponding to
254 the periods of eruptions: December 2009–June 2010 for Type A1, July 2010–September 2011
255 for Type A2, and September 2017–December 2018 for Type B1. $N_i(T_{\text{start}} < t < T_{\text{end}})$ is the
256 number of detected earthquakes in the period. Then, if CR is over the threshold of each type
257 (see Table 1), the template earthquake is classified into the type. We determine the types of the
258 template earthquakes from the top to the bottom in Table 1. When CRs are not over than
259 thresholds of any type, the template events are classified into Type B2. When a template fits
260 two or more types, the template is classified into the topmost type along Table 1. We do not
261 classify template earthquakes for which less than eight DLF earthquakes were detected. Finally,

262 all detected earthquakes are classified according to the types of the template earthquakes that
263 detected them. In other words, the DLF earthquakes concentrated between December 2009 and
264 June 2010 are classified into Type A1; those between July 2010 and September 2011 into Type
265 A2 (Figures 5b and c); those which were activated in the period of the 2018 eruptions into Type
266 B1 (Figure 5d); and those occurring constantly from 2004 to 2018 into Type B2 (Figure 5e).
267 　　　As the result of classification, the number of Type A2 earthquakes is the largest of all
268 types in our classification (Table 1). Additionally, the numbers of Types A1 and B1 are smaller
269 than those of Types A2 and B2. To reveal the causes of these differences, we show the relocated
270 hypocenters in Figure 6. The DLF earthquakes of Type A1 are located around and within the
271 largest cluster at a depth of 22 km and Type A2 are deeper than the other types. Type A2 are
272 separated into three clusters by their spatial distributions (A2.1–A2.3); therefore, we discuss
273 the differences in DLF seismicity in each cluster in subsection 4.3. Types A1 and A2.3
274 earthquakes are located farther northern than any other type. Types B1 and B2 compose the
275 largest cluster together and are not clearly separated from each other. In addition, some of DLF
276 earthquakes at depths of 12 km are classified into Type B2.
277 　　　Waveforms of DLF earthquakes have large variations and are complicated. However,
278 the differences in the waveforms between the types are clear. In particular, Type A2
279 earthquakes have the lowest dominant frequency at approximately 1 Hz, and they show no or
280 small onsets of P waves (Figure 7). The other types (Types A1, B1, and B2) have higher
281 dominant frequencies at approximately 3 Hz and show clear P wave onsets. Furthermore, the
282 earthquakes of Type A1 have a lower dominant frequency than those of Types B1 and B2.
283 Most of the earthquakes of Type A2 clearly have lower dominant frequencies and larger ratios
284 of the amplitudes of S waves to P waves, that is, the typical P wave of Type A2 is weaker than
285 those of the others (Figure 8).
286
287 4.3 DLF seismicity in the activation period including the 2011 eruptions
288 　　　In subsection 4.2, the DLF earthquakes were classified according to time variabilities
289 of the detected earthquakes, and Type A2 were further separated into three clusters (A2.1–
290 A2.3) by their spatial distributions. Thus, we attempt to find differences of DLF seismicity by
291 the clusters.
292 　　　Small clusters of Type A2 are located at depths of 23 km and 25 km (A2.1–A2.3 in
293 Figure 6). The clusters of A2.1, A2.2, and A2.3 include four, one, and five template DLF
294 earthquakes. The characteristics of temporal DLF activity are different depending on the
295 clusters (Figure 9). In other words, Types A2.1, A2.2, and A2.3 had their own activation
296 periods. As explained above, Types A2.1–A2.3 were first separated based on their spatial
297 distributions but they also differ by the characteristics of time variabilities.
298 　　　Type A2.1 increased from August 2010 (Figures 9a–c). In two template earthquakes of
299 Type A2.1, three swarms of DLF earthquakes were observed on August 2010, December 2010,
300 and February 2011. Type A2.2 also increased from August 2010 and gradually from December
301 2010 (Figure 9d). On the other hand, Type A2.3 were observed from December 2010 and
302 activated after the subplinian eruptions (Figures 9e–i).
303 　　　Figures 10a and 10b show the numbers of DLF earthquakes every 14 days, and the
304 ratios of the earthquakes of Types A1 and A2.1–A2.3. The transitions of the four DLF types
305 are consistent with the changes in eruption styles (Figure 10c). The first stage of the eruption
306 was the phreatic stage from 2008 to July 2010 [Nakada et al., 2013; Suzuki et al., 2013]. In this
307 stage, Type A1 mainly occurred. In August 2010, a swarm of Type A2.1 was observed without
308 eruptions. Although Types A2.2 and A2.3 also appear, those numbers were not large. In
309 December 2010, DLF swarms occurred again and included many earthquakes of Type A2.3 at
310 this time. On January 26–27, 2011, the subplinian eruptions occurred and were followed by
311 lava accumulation events [Nakada et al., 2013], but the number of DLF earthquakes is small.

312 In this period, the ratio of Type A2.2 is larger than those in the other time periods. Following
313 the subplinian eruptions, vulcanian eruptions and a swarm of DLF earthquakes occurred in
314 February 2011. After the swarm, Type A2.3 increased and lasted until approximately
315 September 2011. From June 2011, phreatomagmatic eruptions occurred and Type A1 increased
316 again. After the eruptions, Types A1 and A2 were not observed.
317

318 **5 Discussion**

319 5.1 Deep volcanic structure and hypocenters of DLF earthquakes
320 As explained in section 3, the relocated hypocenters of DLF earthquakes are
321 concentrated in the shallow spot at a depth of 10–15 km and the deep spot at a depth of 20–27
322 km. Our result shows that the scattering of the hypocenters in each spot is smaller than in the
323 original catalog of the JMA. It should be noted that DLF earthquakes are distributed not
324 continuously, but separately, in a vertical direction. In addition, hypocenters of DLF
325 earthquakes can be separated into some small isolated sources in both shallow and deep spots,
326 based on classification analysis by their seismicity and relocated hypocenters. Vertical
327 discontinuous distributions of DLF earthquakes were also observed at Laacher See volcano in
328 Germany and Iwate volcano in Japan [Nakamichi et al., 2003; Hensch et al., 2019]. Although
329 these previous studies showed 5–20 km scale separation in the vertical discontinuous
330 distribution, our study in Kirishima volcanoes indicated a separation of a few hundred meters.
331 Results in Kirishima volcanoes suggest that many sources of DLF earthquakes are distributed
332 with various separations at spatial scales of a few hundred meters to 10 km. Those vertical
333 isolated distributions of DLF sources suggest that the distributions correspond to not only
334 large-scale heterogeneities but also small-scale heterogeneities. One of the candidates of such
335 small heterogeneities is sill-like magma. Petrological studies suggest that sill-like magmas
336 inject in various depths in deep crust near the Moho discontinuity [Annen et al., 2006; Cashman
337 et al., 2017]. DLF earthquakes may occur in or around such horizontal magma-sills.
338 Hypocenters of DLF earthquakes also correspond to large-scale heterogeneities.
339 Yamamoto and Ida [1994] and Nagaoka et al. [2018] showed a low-velocity zone beneath
340 Kirishima volcanoes using seismic tomography and interferometry. The low-velocity zone is
341 located beneath a depth of 5–15 km. According to Zhao et al. [2018], another low-velocity
342 zone is located between 20 km and 35 km. These two low-velocity zones roughly correspond
343 to the depths of DLF earthquakes. Furthermore, the observations are consistent with the idea
344 that DLF earthquakes occur in or around low-velocity zones in many volcanoes [Hasegawa et
345 al., 2005; Nakajima, 2017; Shina et al., 2018]. We may interpret that hypocenters of DLF
346 earthquakes at Kirishima volcanoes may be concentrated at many small sources such as small
347 magma reservoirs located in or around the magma sills in the low-velocity zones (Figure 11).
348 In Kirishima volcanoes, DLF earthquakes have not been observed at 30 km depth,
349 which is equivalent to the Moho discontinuity [Matsubara et al., 2017]. The absence of DLF
350 earthquakes on Moho discontinuity may be explained by one or two of the following two
351 hypotheses. One is that the depth of the Moho discontinuity may locally be shallower than 30
352 km due to the existence of the volcano. The other is that the density contrast around the Moho
353 discontinuity is small. However, we cannot verify the hypothesis because the resolution of the
354 estimated velocity structure is not sufficiently detailed.
355
356
357 5.2 DLF earthquakes associated with the eruptions
358
359 DLF earthquakes in the shallow spot did not increase around the 2011 and 2018
360 eruptions unlike those in the deep spot (Figure 3d, 3e). Many previous studies proposed the

361   hypothesis that DLF earthquakes are affected by the movement of fluid [Aki and Koyanagi,
362   1981; Hasegawa et al., 2005; Hotovec-Ellis et al., 2018; Hensch et al., 2019], our results
363   suggest that the fluid movement occurred near the clusters at 20–25 km. Alternatively, no
364   increase in DLF earthquakes in the shallow spot suggests that the fluid did not pass near it.
365   Therefore, one reasonable interpretation of the shallow spot is that it is located along the
366   conduit, connected not to Shinmoe-dake but to Ohachi volcano, which did not erupt in the
367   periods (Figure 11a). This is consistent with the idea of Kagiyama [1994] regarding
368   magnetoelectric and petrological observations that Ohachi volcano can have a different magma
369   supply system from the depth of approximately 20 km. The spatial pattern in the DLF
370   seismicity suggests that the fluid path directly connects to the pressure source at 8 km and the
371   deep spot of DLF earthquakes.
372        We here discuss the detailed seismicity of the DLF earthquakes in the deep spot
373   corresponding to the 2011 eruptions. The hypocenters of Type A2 are deeper than the others
374   obtained by the NCC method. Type A2 earthquakes may have certainly occurred at
375   approximately 23–25 km, which are deeper than those of the other DLF earthquakes. However,
376   the deep locations of the DLF earthquakes associated with the 2011 eruptions can also be
377   interpreted as follows: these DLF earthquakes occurred at the same depths as the other DLF
378   earthquakes, but they were overestimated due to the possible decrease in P- and S-wave
379   velocities by volcanic activity. However, this interpretation is inconsistent with Type B2,
380   which continuously occurred even during the eruption sequences. Thus, it is reasonable that
381   Type A2 actually occurred at the deep locations.
382        Type A1 first increased from December 2009 in the period of phreatic eruptions and
383   was followed by the increase in Type A2 before the subplinian eruptions (Figure 10). In this
384   sequence, Type A1 first occurred at a depth of 21.5 km in the period of phreatic eruptions.
385   Next, Types A2.1 were activated at about 23 km without eruptions. Finally, Type A2.2 and
386   A2.3 were activated at approximately 25 km after the subplinian eruptions (Figure 12). These
387   results in the four clusters suggest that the movement of fluid at the depths may have been
388   triggered from shallower part and switched three times with transitions of eruption styles. We
389   consider that fluid movement probably started beneath the magma reservoir before the
390   subplinian eruptions. Reduction in pressure, which possibly occurred at the depth of 10–20 km,
391   might have triggered the ascent of fluid from the deep crust. Tomiya et al. [2013] proposed that
392   magma mixing process, which might trigger the 2011 subplinian eruptions, occurred 0.4 and 3
393   days before the eruptions in the shallow magma chamber. Magma mixing process might be
394   affected by injection of magma from deep part. Although there were no significant activities
395   of DLF earthquakes directly corresponding to the estimated timing of magma mixing 0.4 and
396   3 days before the eruptions, however, swarms of DLF earthquakes in August and December
397   2010 suggest the change of injection rates of magma.  In addition, the peak of DLF seismicity
398   appeared after the subplinian eruptions on 26-27 January 2011 (Figure 4). These observation
399   results can be explained by the repressurization of the magma reservoir [Segall, 2016]. These
400   complex time-variable activities in many depths were also observed at Laacher See volcano
401   [Hensch et al., 2019]. The result in Kirishima volcanoes that DLF seismicity is different even
402   if the hypocenters are close each other provides an idea that there are many fluid paths forming
403   a network and they sometimes switch. In the network of paths, there are some sources of DLF
404   earthquakes such as small magma reservoirs corresponding to magma intrusions. DLF
405   earthquakes are perhaps observed only when the fluid passes near sources such as small magma
406   reservoirs.
407        While Types A1 and A2 were activated associated with the 2011 eruptions, Type B1
408   were associated with the 2018 eruptions (see Figure 5d). This result suggests that the fluid path
409   of the 2018 eruptions may have differed from that of the 2011 eruptions (Figure 12e). The
410   dominant frequencies of Type B1 is same as those of type B2. Therefore, low-frequency

411 content of Type A2 may not be attributed to the fluid intrusion or heating but to the structure
412 around the hypocenters of type A2 earthquakes.
413      The concentration of DLF earthquakes in Kirishima volcanoes suggests that DLF
414 earthquakes occur at specific locations, such as near magma reservoirs. Therefore, we consider
415 a model similar to the trigger and resonant model proposed for volcanic shallow low-frequency
416 earthquakes [Neuberg et al., 2006]. The earthquakes occurred near the surface; however, the
417 waveforms of the shallow low-frequency earthquakes, which have dominant frequencies of
418 approximately 1–10 Hz and a long coda wave, are similar to those of DLF earthquakes. The
419 fluid-filled crack model [Aki et al., 1977], one of the shallow low-frequency earthquake models,
420 can also explain the characteristics of DLF earthquakes. There is a problem as to why
421 earthquakes occur at a depth in which no regular earthquakes have been observed. It may be
422 explained to consider similar model to the cooling magma model in which thermal strain causes
423 brittle failure, and waves are trapped in the resonance [Aso and Tsai, 2014]. If the cooling of
424 magma trigger DLF earthquakes, heating of magma by the fluid flow may also trigger the
425 earthquakes and this model can explain the activation of DLF earthquakes associated with
426 eruptions in Kirishima volcanoes.

428 5.3 Possibility to predict eruptions by monitoring DLF earthquakes

430      It is well known that long-period earthquakes, which occur near the surface, are useful
431 for predicting eruptions [Chouet, 1996]. However, if DLF earthquakes are also available, the
432 prediction accuracy will be improved by combining the observations of regular and DLF
433 earthquakes. This study reveals that a large number of unique DLF earthquakes occurred before
434 the 2011 subplinian eruptions and it suggests that monitoring DLF earthquakes may also be
435 useful to predict eruptions in the future. One factor making it difficult to use DLF earthquakes
436 for prediction is their diversity. DLF earthquakes in 2011 and 2018 exhibit many different
437 characteristics of locations and waveforms; hence, we cannot predict at this moment how DLF
438 earthquakes will occur prior to the next eruption. The matched filter technique can only detect
439 the earthquakes that have waveforms and locations similar to those of template earthquakes.
440 Thus, another method not depending on templates is necessary for the prediction.

442 **6 Conclusions**

443      We analyzed DLF earthquakes that occurred at depths of 10–30 km in Kirishima
444 volcanoes and found following features:
445 1. Relocated hypocenters of DLF earthquakes show that the earthquakes are concentrated in
446 small clusters at the depths of 10–15 km and 20–27 km in low-velocity zones.
447 2. Activations of DLF earthquakes at depths of 20–27 km associated with the 2011 and 2018
448 eruptions were observed.
449 3. The activation with the 2011 eruptions had been observed for approximately two years since
450 December 2009, associated with crustal deformation.
451 4. Waveforms of the DLF earthquakes associated with the 2011 eruptions had lower dominant
452 frequencies and weak P waves.
453 5. Most hypocenters of DLF earthquakes associated with the 2011 eruptions were concentrated
454 in four deeper clusters which are different from those of the other earthquakes, and active
455 clusters were switched three times with transitions of eruption styles.
456 6. The waveforms and hypocenters of DLF earthquakes associated with the 2018 eruptions are
457 almost the same as those of the earthquakes which constantly occurred from 2004 to 2018.
458      The concentrated locations suggest that DLF earthquakes can occur only in particular
459 locations, such as small magma reservoirs near magma sills. The activations of DLF

460 earthquakes may reflect the fluid flow in the deep crust. In addition, different locations of DLF
461 earthquakes for the 2011 and 2018 eruptions suggest that the fluid paths are different. These
462 results show the possibility that eruption processes are directly related to fluid flow in the deep
463 crust.
464

**References**

479 Aki, K., Fehler, M., & Das, S. (1977). Source mechanism of volcanic tremor: fluid-driven
480 crack models and their application to the 1963 Kilauea eruption. Journal of Volcanology and
481 Geothermal Research, 2(3), 259–287. https://doi.org/10.1016/0377-0273(77)90003-8
482
483 Aki, K., & Koyanagi, R. (1981). Deep volcanic tremor and magma ascent mechanism under
484 Kilauea, Hawaii. Journal of Geophysical Research, 86(B8), 7095–7109.
485
486 Annen, C., Blundy, J. D., & Sparks, R. S. J. (2006). The genesis of intermediate and silicic
487 magmas in deep crustal hot zones. Journal of Petrology, 47(3), 505–539.
488 https://doi.org/10.1093/petrology/egi084
489
490 Aso, N., Ohta, K., & Ide, S. (2013). Tectonic, volcanic, and semi-volcanic deep low-
491 frequency earthquakes in western Japan. Tectonophysics, 600, 27–40.
492 https://doi.org/10.1016/j.tecto.2012.12.015
493
494 Aso, N., & Tsai, V. C. (2014). Cooling magma model for deep volcanic long-period
495 earthquakes. Journal of Geophysical Research: Solid Earth, 119(11), 8442–8456.
496 https://doi.org/10.1002/2014JB011180
497
498 Cashman, K. V., Sparks, R. S. J., & Blundy, J. D. (2017). Vertically extensive and unstable
499 magmatic systems: A unified view of igneous processes. Science, 355(6331).
500 https://doi.org/10.1126/science.aag3055
501

502 Chouet, B. A. (1996). Long-period volcano seismicity: its source and use in eruption
503 forecasting. Nature, 380(6572), 309–316. https://doi.org/10.1038/380309a0

504

505 Frank, W. B., Shapiro, N. M., & Gusev, A. A. (2018). Progressive reactivation of the
506 volcanic plumbing system beneath Tolbachik volcano (Kamchatka, Russia) revealed by long-
507 period seismicity. Earth and Planetary Science Letters, 493, 47–56.
508 https://doi.org/10.1016/j.epsl.2018.04.018

509

510 Funasaki, J., & Earthquake Prediction Information Division. (2004). Revision of the JMA
511 velocity magnitude. Quarterly Journal of Seismology, 67(1–4), 11–20. (in Japanese with
512 English abstract)

513

514 Gibbons, S. J., & Ringdal, F. (2006). The detection of low magnitude seismic events using
515 array-based waveform correlation. Geophysical Journal International, 165: 149–166.
516 https://doi.org/10.1111/j.1365-246X.2006.02865.x

517

518 Hasegawa, A., Nakajima, J., Umino, N., & Miura, S. (2005). Deep structure of the
519 northeastern Japan arc and its implications for crustal deformation and shallow seismic
520 activity. Tectonophysics, 403(1–4), 59–75. https://doi.org/10.1016/j.tecto.2005.03.018

521

522 Hensch, M., Dahm, T., Ritter, J., Heimann, S., Schmidt, B., Stange, S., & Lehmann, K.
523 (2019). Deep low-frequency earthquakes reveal ongoing magmatic recharge beneath Laacher
524 See Volcano (Eifel, Germany). Geophysical Journal International, 216(3), 2025–2036.
525 https://doi.org/10.1093/gji/ggy532

526

527  Hotovec-Ellis, A. J., Shelly, D. R., Hill, D. P., Pitt, A. M., Dawson, P. B., & Chouet, B. A.
528 (2018). Deep fluid pathways beneath Mammoth Mountain, California, illuminated by
529 migrating earthquake swarms. Science Advances, 4(8), eaat5258.
530 https://doi.org/10.1126/sciadv.aat5258

531

532 Japan Meteorological Agency (2018).  Volcanic activity of Kirishimayama volcano –
533 February 1, 2018 – May 31, 2018–. Report of Coordinating Committee for Prediction of
534 Volcanic Eruption, 130, 213-284. (in Japanese)

535

536 Kagiyama, T. (1994). Kirishima volcanoes – Multi active volcanic group generated in a
537 slightly tensile stress field. Journal of Geography, 103(5), 479–487. (in Japanese with English
538 abstract)

539

540 Katsumata, A., & Kamaya, N. (2003). Low-frequency continuous tremor around the Moho
541 discontinuity away from volcanoes in the southwest Japan. Geophysical Research Letters,
542 30(1), 1020. https://doi.org/10.1029/2002GL015981

543

544 Kosuga, M., Noro, K., & Masukawa, K. (2017). Characteristics of spatiotemporal variations
545 of hypocenters and diversity of waveforms of deep low-frequency earthquakes in
546 northeastern Japan. Bulletin of the Earthquake Research Institute, University of Tokyo, 92,
547 63–80. (in Japanese with English abstract)

548

549 Matsubara, M., Sato, H., Ishiyama, T., & Van Horne, A.D. (2017). Configuration of the
550 Moho discontinuity beneath the Japanese Islands derived from three-dimensional seismic
551 tomography. Tectonophysics, 710–711, 97–107, https://doi.org/10.1016/j.tecto.2016.11.025

552

553 Nagaoka, Y., Nishida, K., Aoki, Y., Takeo M., Ohkura S., & Yoshikawa, S. (2018). $V_{SV}$ and
554 $V_{SH}$ structure beneath Kirishima volcanoes inferred from seismic interferometry. Japan
555 Geophysical Union Meeting 2018, SVC41-44 (Abstract)

556

557 Nakada, S., Nagai, M., Kaneko, T., Suzuki, Y., & Maeno, F. (2013). The outline of the 2011
558 eruption at Shinmoe-dake (Kirishima), Japan. Earth, Planets and Space, 65(6), 475–488.
559 https://doi.org/10.5047/eps.2013.03.016

560

561 Nakajima, J. (2017). Seismic velocity and attenuation structures around active volcanoes
562 beneath Tohoku: Linking Crustal Structure to Low-frequency Earthquakes and S-wave
563 Reflectors. Bulletin of the Earthquake Research Institute, University of Tokyo, 92, 49–62. (in
564 Japanese with English abstract)

565

566 Nakamichi, H., Hamaguchi, H., Tanaka, S., Ueki, S., Nishimura, T., & Hasegawa, A. (2003).
567 Source mechanisms of deep and intermediate-depth low-frequency earthquakes beneath
568 Iwate volcano, northeastern Japan. Geophysical Journal International, 154(3), 811–828.
569 https://doi.org/10.1046/j.1365-246X.2003.01991.x

570

571 Nakamichi, H., Yamanaka, Y., Terakawa, T., Horikawa, S., Okuda, T., & Yamazaki, F.
572 (2013). Continuous long-term array analysis of seismic records observed during the 2011
573 Shinmoedake eruption activity of Kirishima volcano, southwest Japan. Earth, Planets and
574 Space, 65(6), 551–562. https://doi.org/10.5047/eps.2013.03.002

575

576 Nakao, S., Morita, Y., Yakiwara, H., Oikawa, J., Ueda, H., Takahashi, H., Ohta, Y.,
577 Matsushima, T., & Iguchi, M. (2013). Volume change of the magma reservoir relating to the
578 2011 Kirishima Shinmoe-dake eruption—Charging, discharging and recharging process
579 inferred from GPS measurements. Earth, Planets and Space, 65(6), 505–515.
580 https://doi.org/10.5047/eps.2013.05.017

581

582 National Research Institute for Earth Science and Disaster Resilience (2019). NIED Hi-net,
583 https://doi.org/10.17598/nied.0003

584

585  Neuberg, J. W., Tuffen, H., Collier, L., Green, D., Powell, T., & Dingwell, D. (2006). The
586  trigger mechanism of low-frequency earthquakes on Montserrat. Journal of Volcanology and
587  Geothermal Research, 153(1–2), 37–50. https://doi.org/10.1016/j.jvolgeores.2005.08.008

588

589  Ohta, K., & Ide, S. (2011). Precise hypocenter distribution of deep low-frequency
590  earthquakes and its relationship to the local geometry of the subducting plate in the Nankai
591  subduction zone, Japan. Journal of Geophysical Research, 116, B01308.
592  https://doi.org/10.1029/2010JB007857

593

594  Okada, Y., Kasahara, K., Hori, S., Obara, K., Sekiguchi, S., Fujiwara, H., & Yamamoto, A.
595  (2004). Recent progress of seismic observation networks in Japan —Hi-net, F-net, K-NET
596  and KiK-net—. Earth, Planets and Space, 56(8), xv–xxviii.
597  https://doi.org/10.1186/BF03353076

598

599  Sagiya, T. (2004). A decade of GEONET: 1994-2003 - The continuous GPS observation in
600  Japan and its impact on earthquake studies -. Earth, Planets and Space, 56(8), xxix–xli.
601  https://doi.org/10.1186/BF03353077

602

603  Segall, P. (2016). Repressurization following eruption from a magma chamber with a
604  viscoelastic aureole. Journal of Geophysical Research: Solid Earth, 121(12), 8501–8522.
605  https://doi.org/10.1002/2016JB013597

606

607  Shapiro, N. M., Droznin, D. V, Droznina, S. Y., Senyukov, S. L., Gusev, A. A., & Gordeev,
608  E. I. (2017). Deep and shallow long-period volcanic seismicity linked by fluid-pressure
609  transfer. Nature Geoscience, 10(6), 442–445. https://doi.org/10.1038/ngeo2952

610

611  Shelly, D. R., Beroza, G. C., & Ide, S. (2007). Non-volcanic tremor and low-frequency
612  earthquake swarms. Nature, 446(7133), 305–307. https://doi.org/10.1038/nature05666

613

614  Shiina, T., Takahashi, H., Okada, T., & Matsuzawa, T. (2018). Implications of seismic
615  velocity structure at the junction of Kuril-Northeastern Japan arcs on active shallow
616  seismicity and deep low-frequency earthquakes. Journal of Geophysical Research: Solid
617  Earth, 123(10), 8732–8747. https://doi.org/10.1029/2018JB015467

618

619  Suzuki, Y., Nagai, M., Maeno, F., Yasuda, A., Hokanishi, N., Shimano, T., Ichihara, M.,
620  Keneko, T., & Nakada, S. (2013). Precursory activity and evolution of the 2011 eruption of
621  Shinmoe-dake in Kirishima volcano—insights from ash samples. Earth, Planets and Space,
622  65(6), 591–607. https://doi.org/10.5047/eps.2013.02.004

623

624  Takahashi, H., & Miyamura, J. (2009). Deep Low-Frequency Earthquakes occurring in
625  Japanese Islands. Geophysical Bulletin of Hokkaido University, 72, 177–190. (in Japanese
626  with English abstract)

627

628 Tomiya, A., Miyagi, I., Saito, G., & Geshi, N. (2013). Short time scales of magma-mixing
629 processes prior to the 2011 eruption of Shinmoedake volcano, Kirishima volcanic group,
630 Japan. Bulletin of Volcanology, 75(10), 750. https://doi.org/10.1007/s00445-013-0750-1

631

632 Ukawa, M. (2007). Low frequency earthquakes at Mount Fuji. Fuji Volcano, 161–172. (in
633 Japanese with English abstract)

634

635 Ukawa, M., & Ohtake, M. (1987). A monochromatic earthquake suggesting deep-seated
636 magmatic activity beneath the Izu-Ooshima Volcano, Japan. Journal of Geophysical
637 Research, 92(10), 12,649-12,663. https://doi.org/10.1029/JB092iB12p12649

638

639 Wessel, P., & Smith, W. H. F. (1998). New, improved version of Generic Mapping Tools
640 released. Eos, Transactions American Geophysical Union, 79(47), 579.
641 https://doi.org/10.1029/98EO00426

642

643 White, R. A. (1996). Precursory deep long-period earthquakes at Mount Pinatubo: Spatio-
644 temporal link to a basalt trigger. University of Washington Press, Seattle, Fire and Mud:
645 Eruptions and Lahars of Mount Pinatubo, Philippines. Newhall, C.G., Punongbayan, R.S.
646 (Eds.), 307–326.

647

648 Yamamoto, K., & Ida, Y. (1994). Three-dimensional P-wave velocity structure of Kirishima
649 volcanoes using regional seismic events. Bulletin of the Earthquake Research Institute,
650 University of Tokyo, 69, 267–289. (in Japanese with English abstract)

651

652 Zhao, D., Yamashita, K., & Toyokuni, G. (2018). Tomography of the 2016 Kumamoto
653 earthquake area and the Beppu-Shimabara graben. Scientific Reports, 8(1), 15488.
654 https://doi.org/10.1038/s41598-018-33805-0

655
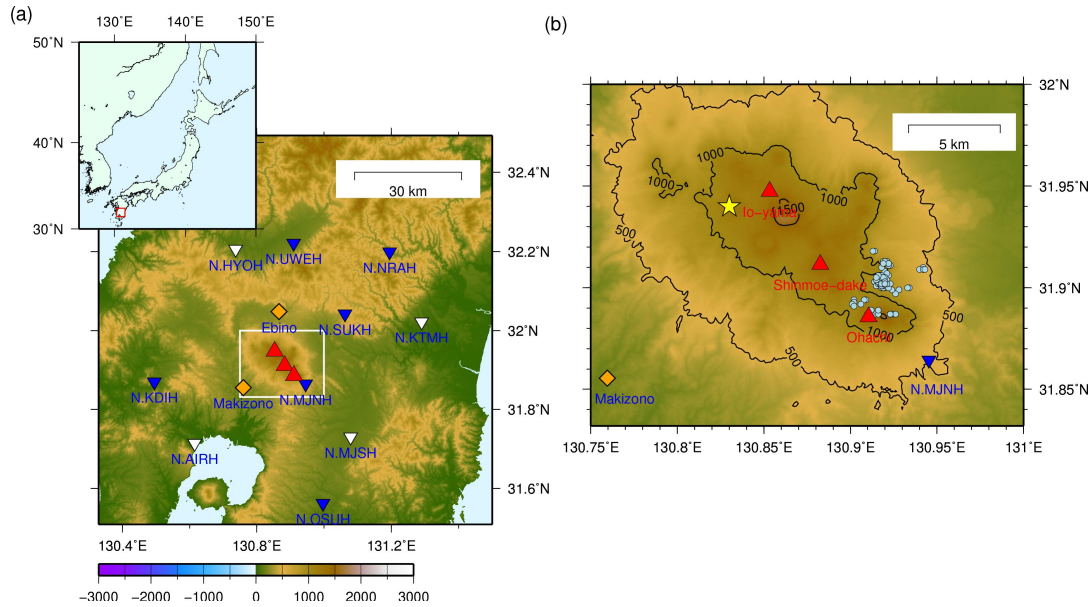
657      Figure 1. (a) Locations of Kirishima volcanoes and observation stations used in this
658 study. Red triangles show the locations of Io-yama, Shinmoe-dake, and Ohachi volcanoes in
659 Kirishima volcanoes. Inversed triangles indicate the locations of Hi-net stations used for
660 relocation and detection (blue) and used only for relocation (white). N.KTMH and N.AIRH
661 stations are also used for detection when one or two blue stations are missing observations.
662 Orange diamonds show the locations of global navigation satellite system (GNSS) stations in
663 GNSS earth observation network system (GEONET) [Sagiya, 2004] operated by Geospatial
664 Information Authority of Japan. (b) Enlarged view in the white rectangle in (a) with the same
665 symbols. In addition, light blue circles show the locations of DLF earthquakes obtained by the
666 relocation discussed in section 3. A yellow star represents the location of the estimated pressure
667 source of the 2011 Shinmoe-dake eruptions at the depths of approximately 8 km [Nakao et al.,
668 2013].

669
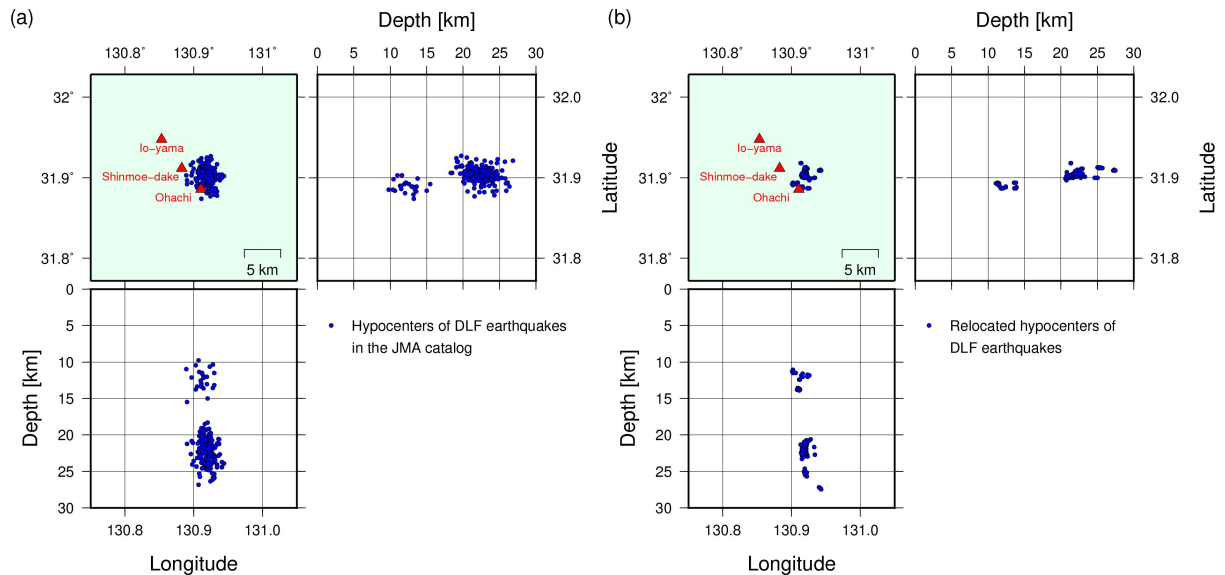


670
671      Figure 2. (a) Three-dimensional distributions of DLF earthquakes in the JMA catalog.
672 Red triangles are the summits of three active volcanoes in the Kirishima volcanoes. Blue circles
673 show the locations of DLF earthquakes, which can be relocated by NCC method. (b) Three-
674 dimensional distribution of the earthquakes after relocation.
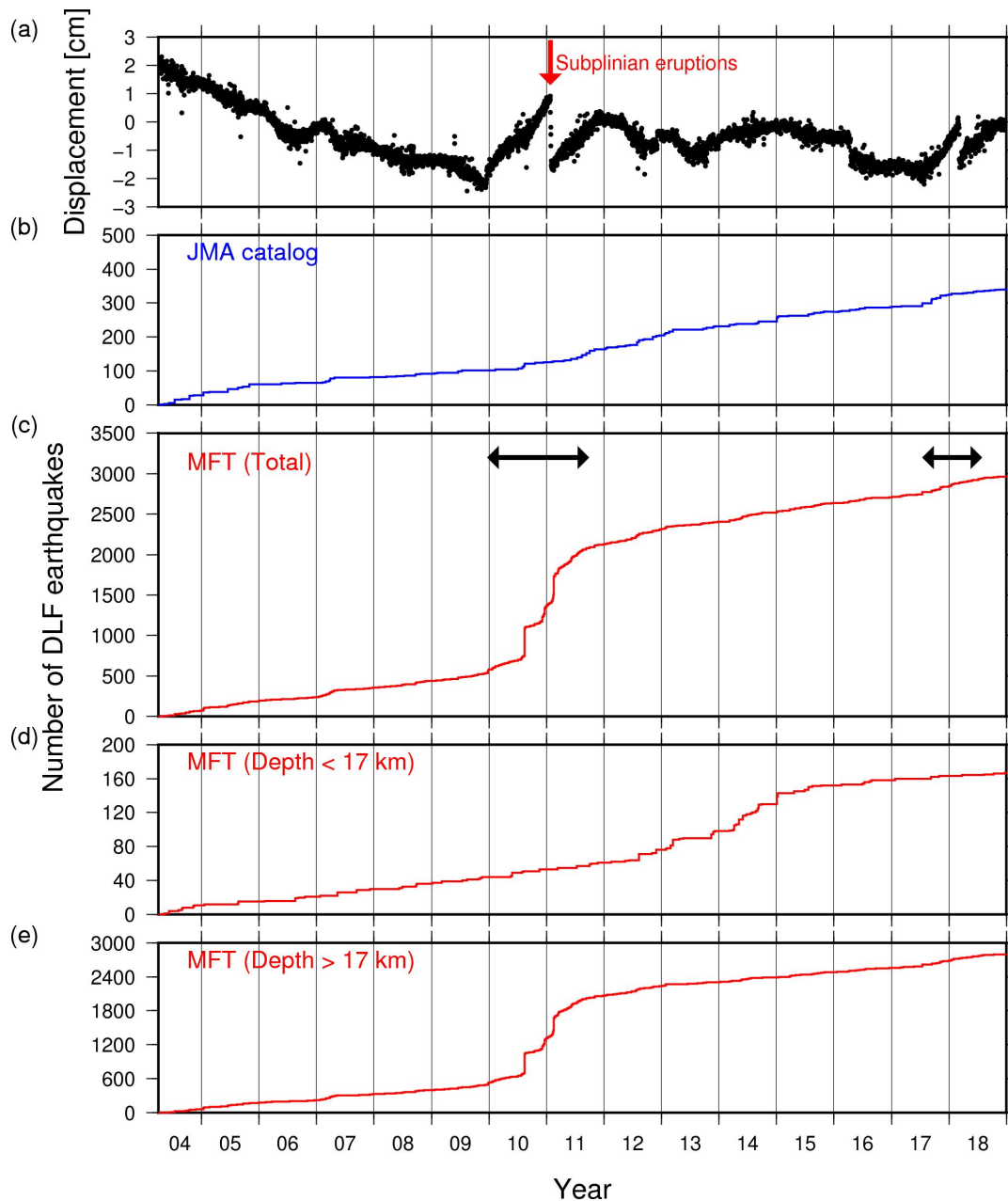
Figure 3. (a) The amount of the horizontal displacement of Ebino relative to Makizono (see Figure 1) calculated from GNSS data. We use F3 solutions provided by Geospatial Information Authority of Japan. (b) A cumulative number of DLF earthquakes in the JMA catalog from April 2004. (c) Cumulative number of DLF earthquakes detected by the matched filter technique (MFT). Black arrows show periods of increasing DLF earthquakes. (d) Cumulative number of DLF earthquakes detected by MFT located shallower than 17 km. (e) Cumulative number of DLF earthquakes detected by MFT located deeper than 17 km.
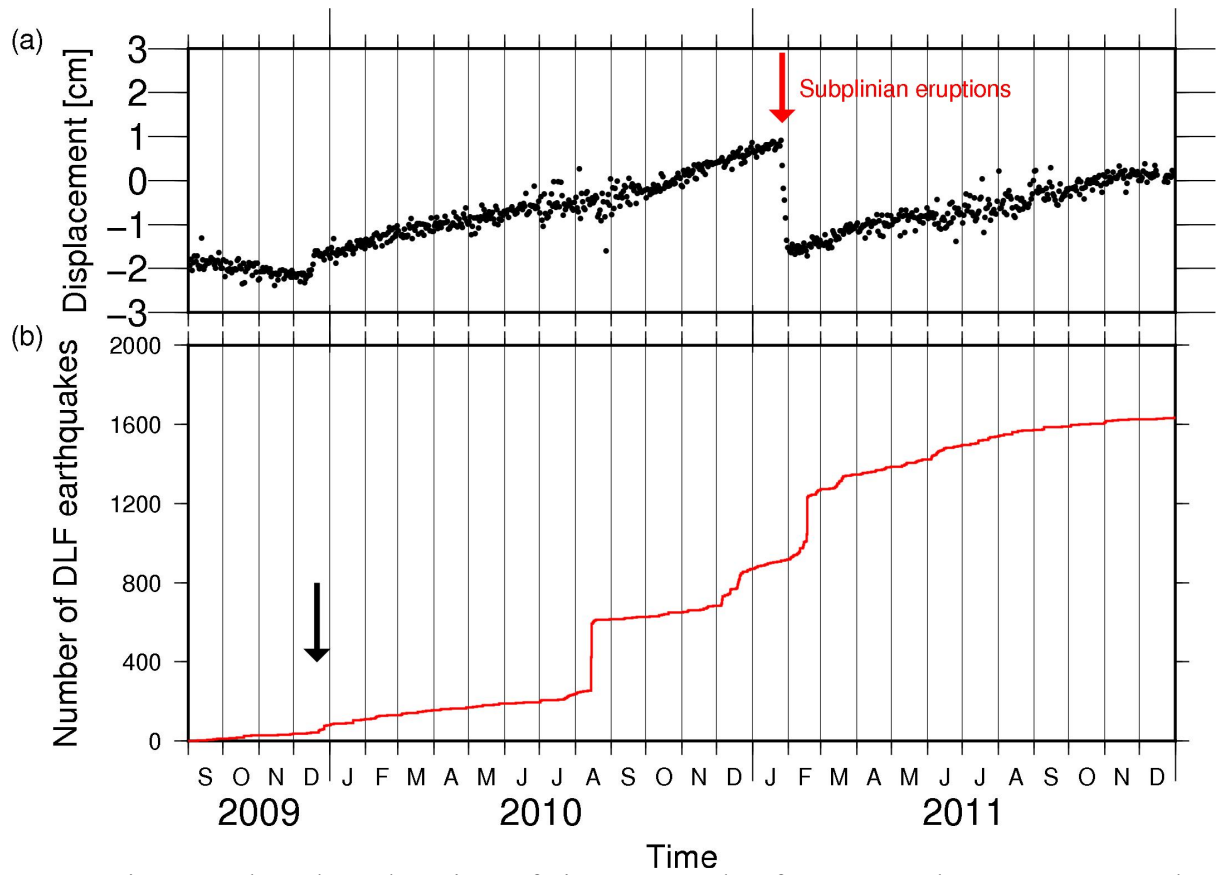
684
685      Figure 4. The enlarged portions of Figures 3a and 3c from September 2009 to December
686      2011. The black arrow shows when increasing of DLF earthquakes initiated.
687
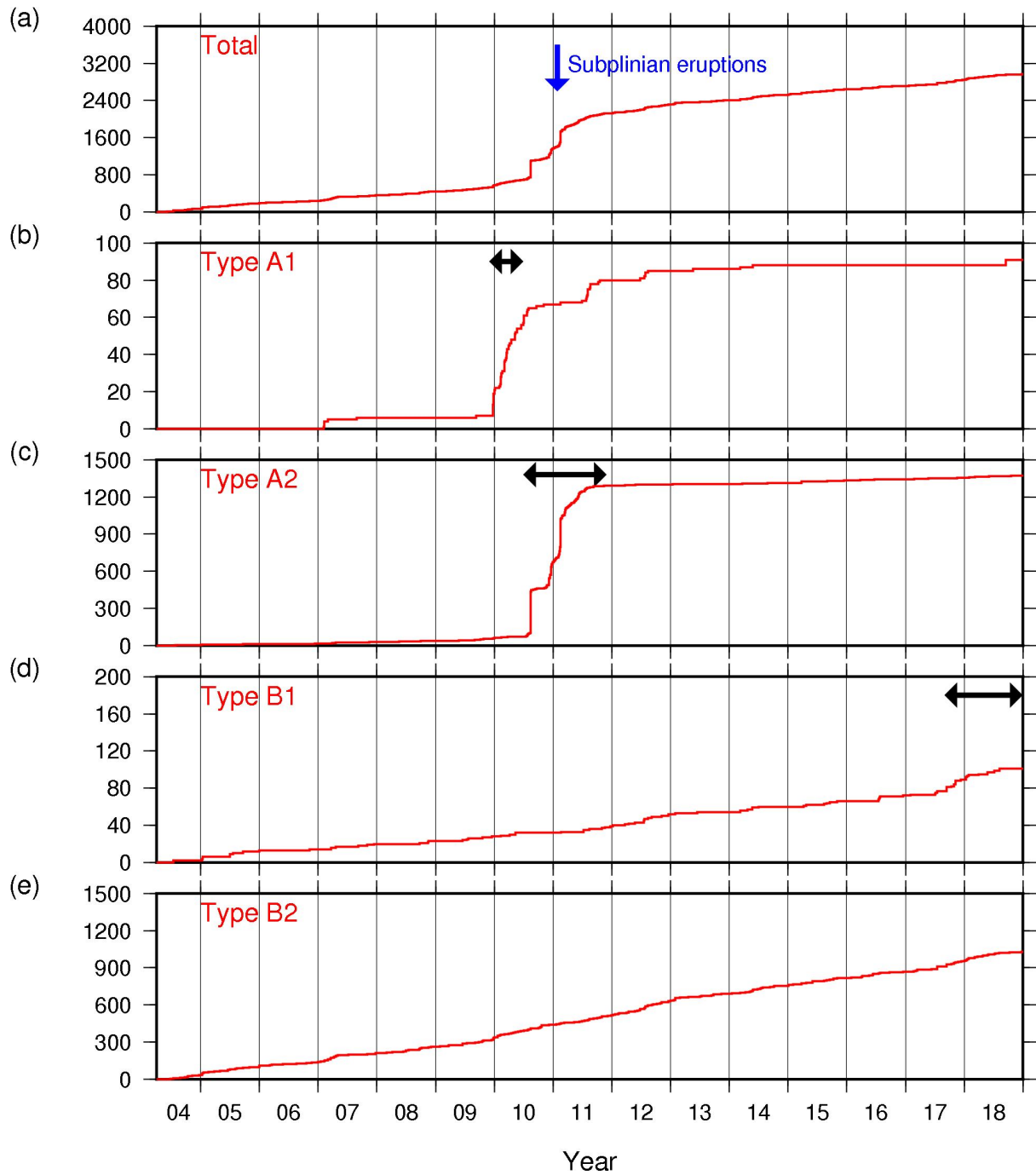
688
689 Figure 5. Cumulative number of DLF earthquakes. (a) Same figure as Figure 3c. (b–e)
690 Total cumulative number of DLF earthquakes classified into each type. Black arrows show the
691 periods in which each type earthquakes are concentrated.
692
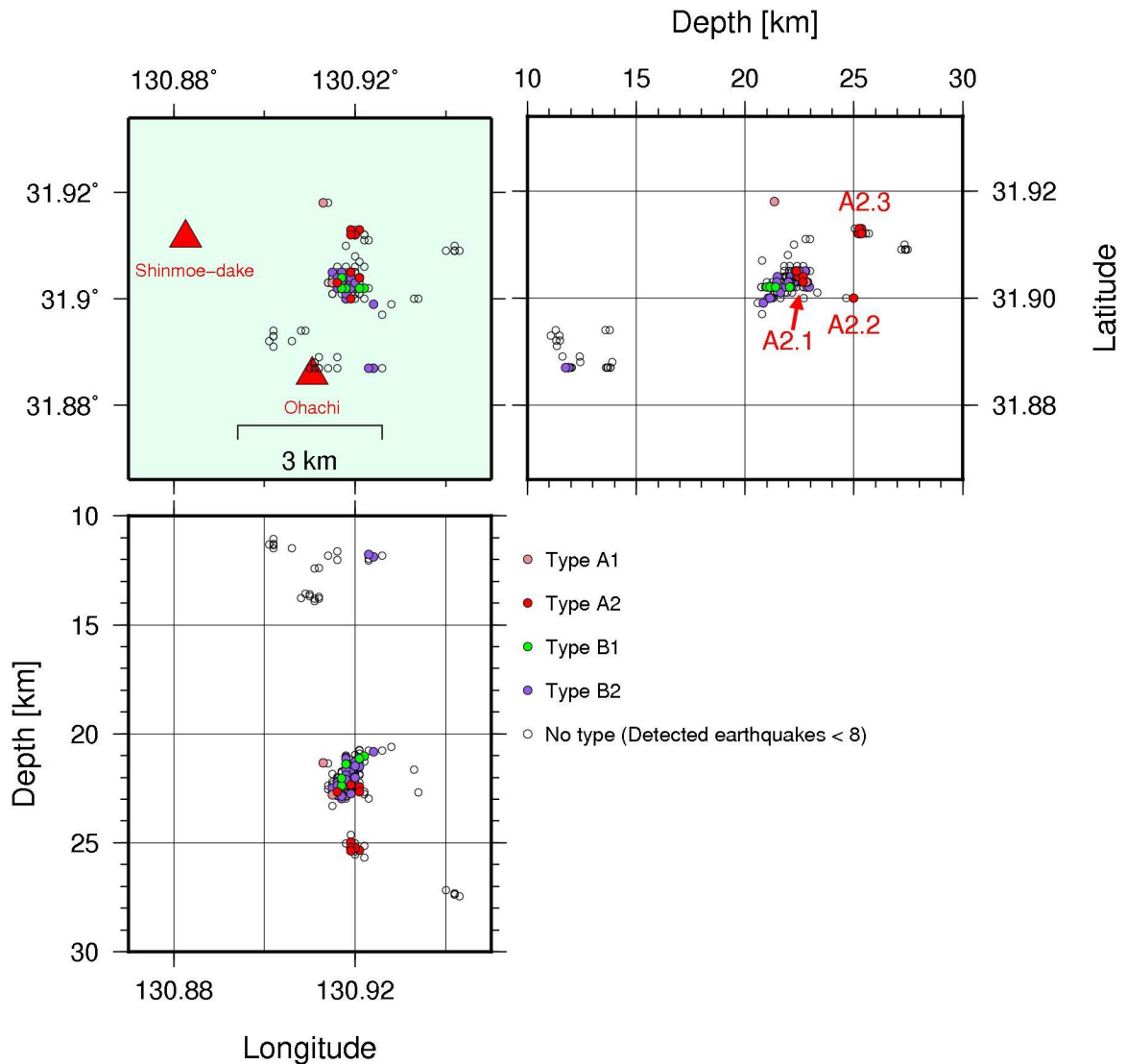
693
694 Figure 6. Three-dimensional distribution of DLF earthquakes. The circles indicate the
695 relocated hypocenters of DLF earthquakes, and the colors of the circles show the types of
696 earthquakes (see Table 1). Red triangles represent the summits of Shinmoe-dake and Ohachi
697 volcanoes. White circles are the relocated but unclassified hypocenters of DLF earthquakes,
698 for which fewer than eight earthquakes were detected. A2.1–A2.3 show the locations of Type
699 A2 earthquakes discussed in subsection 4.3.
700
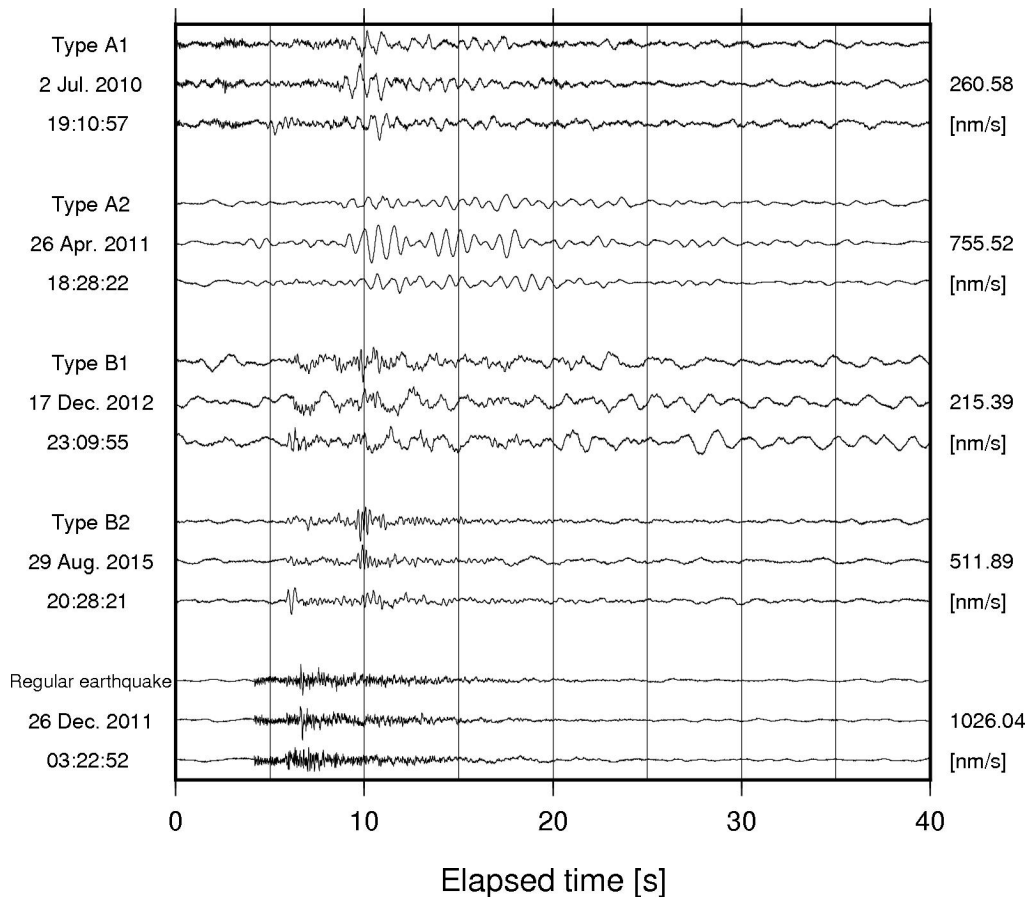
701
702 Figure 7. Three components of typical velocity waveforms of each type of DLF
703 earthquake and a regular earthquake observed at the N.SUKH station (see Figure 1). The three
704 waveforms correspond to the east-west, north-south, and up-down components from the top.
705 The type of DLF earthquake and occurrence time (Japan standard time) are written to the left
706 of the waveforms. All waveforms are normalized by the maximum amplitudes of each
707 earthquake written in right. A bandpass filter is not applied to the waveforms.
708
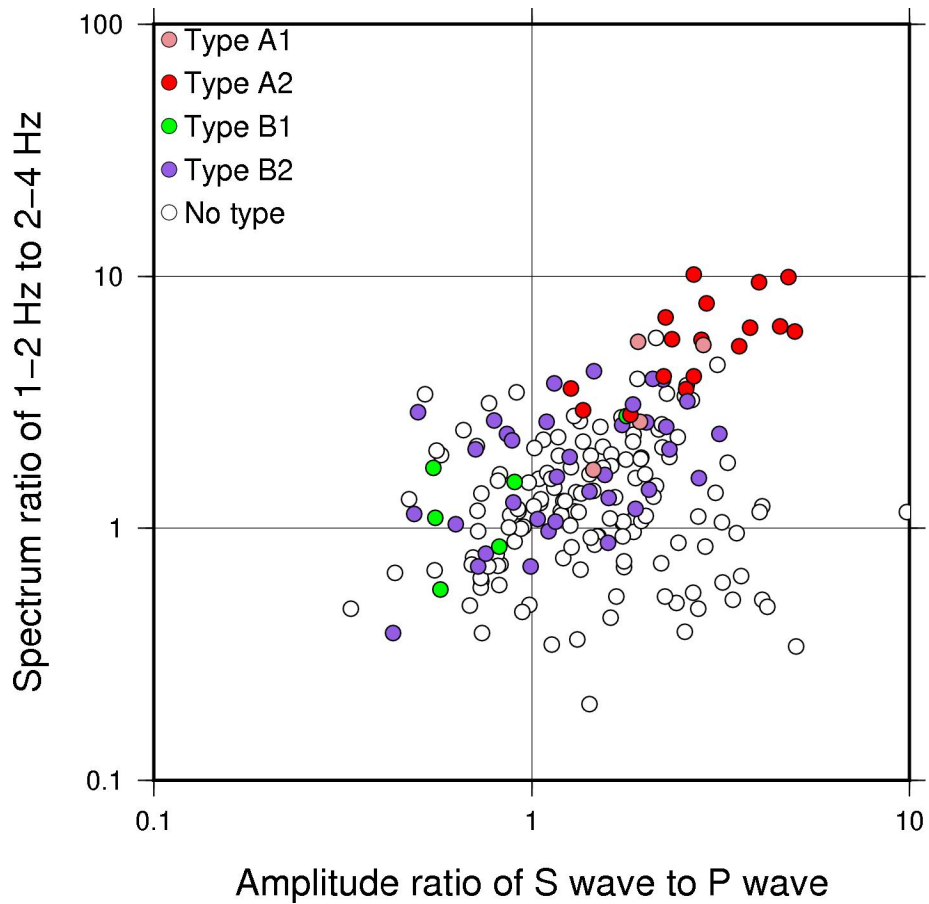
709
710    Figure 8. Distribution of the maximum amplitude ratios of S waves to P waves and the
711    ratios of the average spectrum of 1–2 Hz to 2–4 Hz at N.SUKH station. The circles show the
712    DLF earthquakes, and the colors indicate the types of the earthquakes listed in Table 1.
713
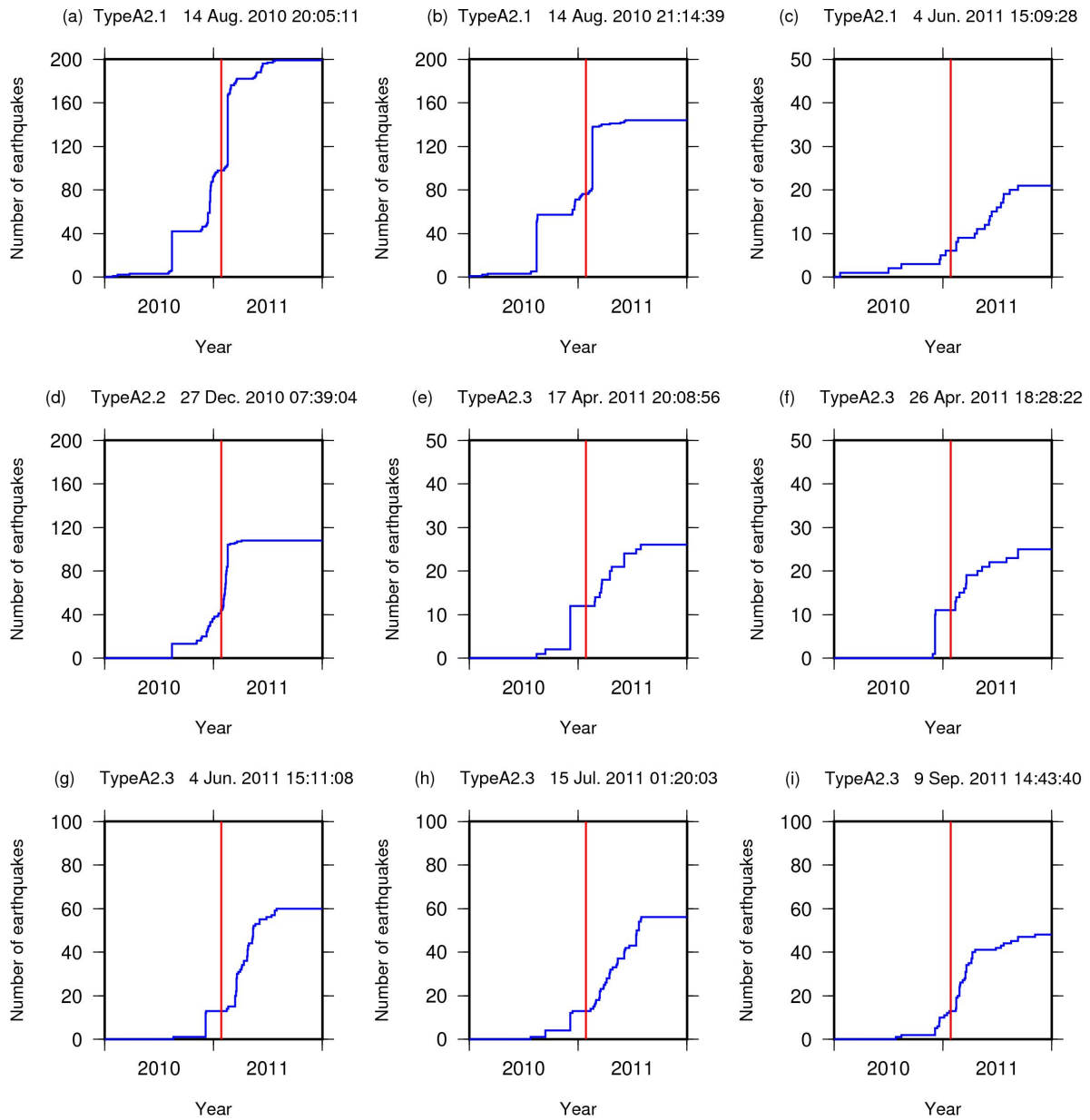
714
715 Figure 9. Cumulative number of DLF earthquakes detected by each template
716 earthquake of Type A2 from January 2010, except the template which detected less than 20
717 earthquakes. Type and occurrence time of each template earthquake are written above the
718 figures. Red lines show the time of the subplinian eruptions of Shinmoe-dake on 26 January
719 2011.
720
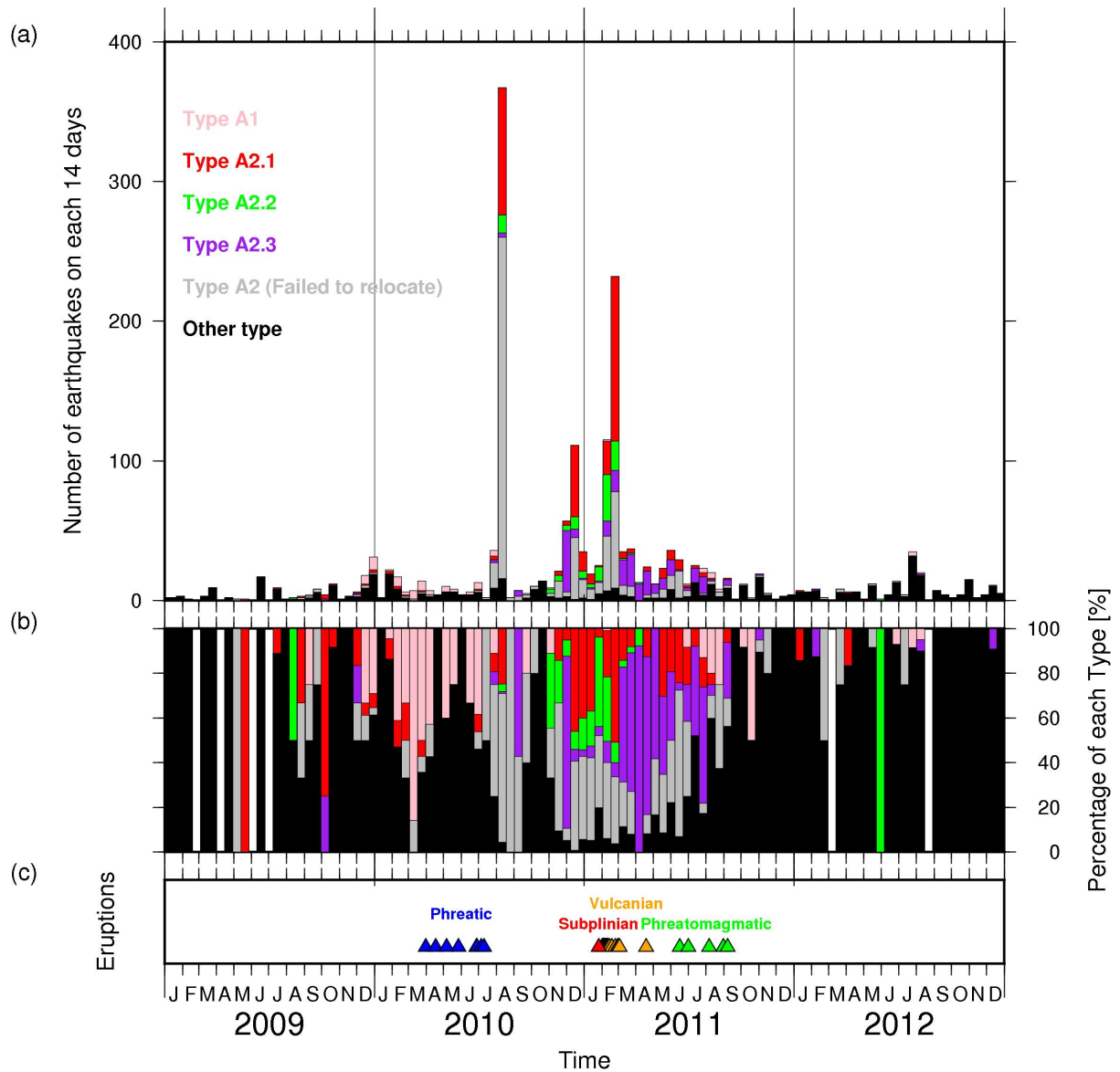
Figure 10. (a) Number of DLF earthquakes in a 14-days time window. Bars show the number of earthquakes, and their colors indicate the types of the earthquakes. (b) Percentages of each type of DLF earthquakes. White lines show the absence of earthquakes in a 14-days time window. (c) The transition of the eruptions of Shinmoe-dake volcano. The times of the eruptions were reported in Nakada et al. [2013]. Eruption stages of less than a few days were excluded.
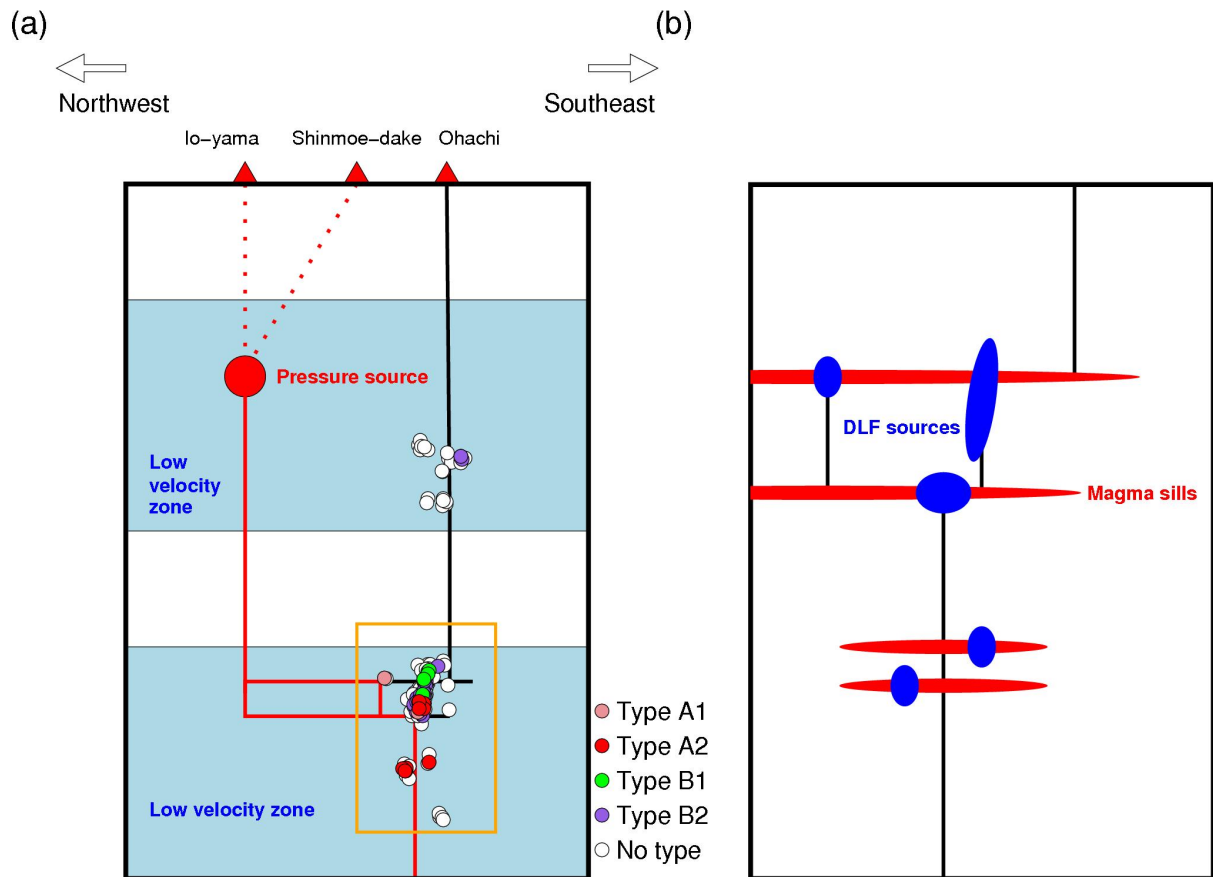
Figure 11. (a) Schematic model of volcanic fluid paths inferred from hypocenters of DLF earthquakes and interaction between DLF earthquakes and surface volcanic activities. A large red circle is the magma reservoir [Nakao et al., 2013]. Colored small circles are hypocenters of DLF earthquakes and the colors show the types of DLF earthquakes as Figures 6 and 8. Red dotted lines represent the conduits for Shinmoe-dake [Nakamichi et al., 2013] and Io-yama from the magma reservoir. Black and red solid lines indicate the estimated paths of magma for the volcanoes based on DLF seismicity. Red lines show the estimated active paths at the 2011 eruptions and black lines show the estimated paths that were not active at the 2011 eruptions. Blue hatches show the low-velocity zone reported in previous studies [Yamamoto and Ida, 1994; Nagaoka et al., 2018; Zhao et al., 2018]. (b) Enlarged model of the fluid paths and magma sills near DLF sources. The area is shown as the orange rectangle in (a). Red horizontal lines show the magma sills and vertical lines show conduits. Blue ellipses show the sources of DLF earthquakes such as magma reservoirs.
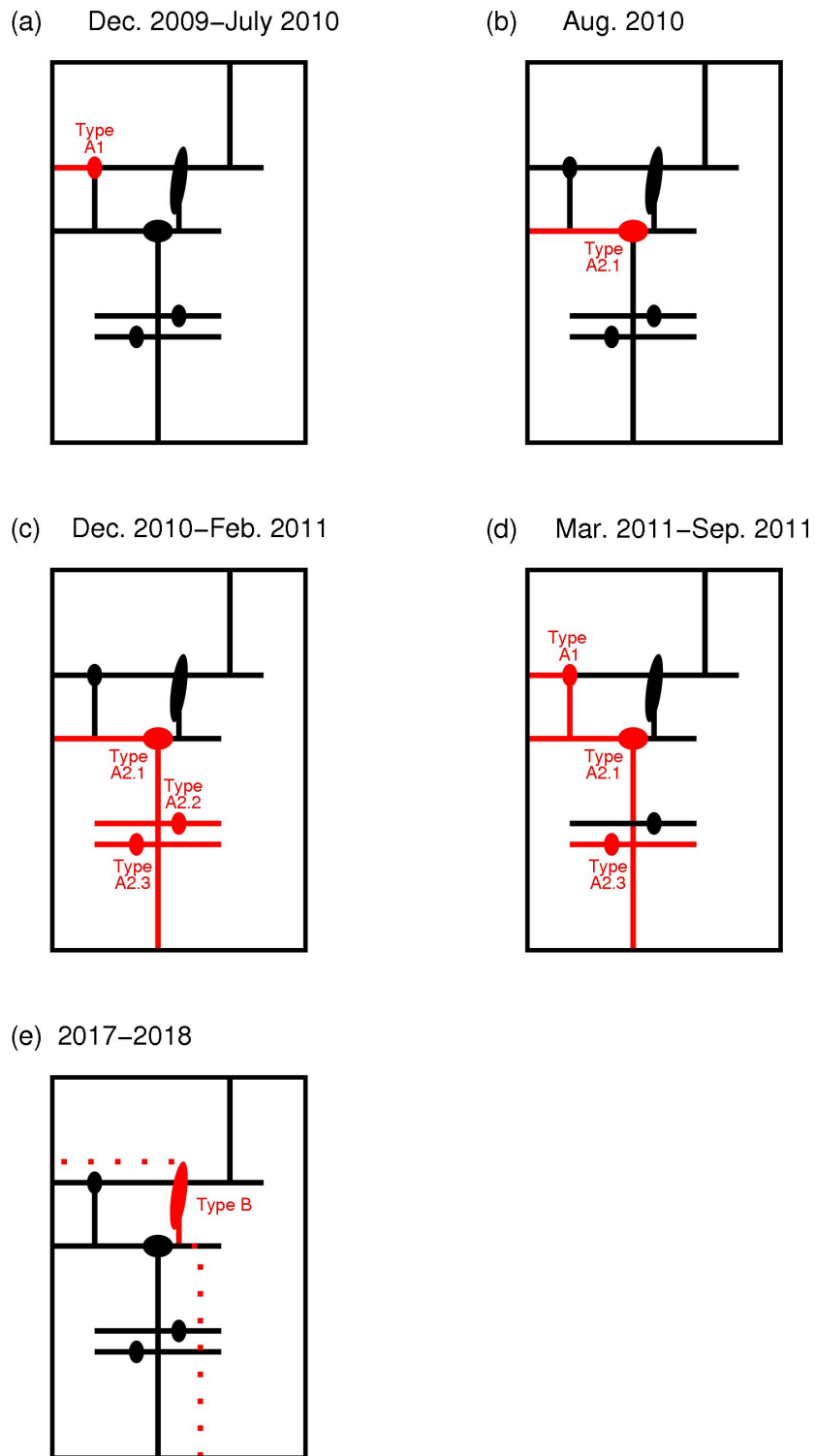
Figure 12. Distribution of DLF earthquakes and estimated fluid flow paths on each term, in which swarms or increases in DLF earthquakes occurred. (a)–(d) are in terms of the 2011 eruptions, December 2009–July 2010, August 2010, December 2010–February 2011, and March 2011–September 2011, respectively, and (e) for the 2017–2018 eruptions. The area is same as Figure 11(b). Red and black lines show the active and non-active paths of fluid estimated from the activities of DLF earthquakes in each term, respectively. Red dotted lines in (e) show imaginary magma paths in the period of 2017–2018 eruptions. Ellipses show the sources of DLF earthquakes such as magma reservoirs.

754

755    Table 1. Definition and number of each type of DLF earthquakes.

| Type of DLF earthquakes | Periods | Thresholds of CR | Number of template earthquakes (Relocated earthquakes) | Number of detected earthquakes |
|---|---|---|---|---|
| A1 | December 2009-June 2010 | 0.4 | 4 (2) | 91 |
| A2 | July 2010-September 2011 | 0.4 | 17 (10) | 1373 |
| B1 | September 2017-December 2018 | 0.2 | 6 (6) | 101 |
| B2 | All template earthquakes except above | | 36 (32) | 1027 |
| No type | Detected earthquakes < 8 or not used for MFT | | 212 (152) | 372 |

756